

RICE UNIVERSITY

**Development of Image Mapping Spectrometer
(IMS) for hyperspectral fluorescence microscopy**

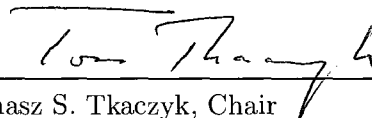
by

Liang Gao

A THESIS SUBMITTED
IN PARTIAL FULFILLMENT OF THE
REQUIREMENTS FOR THE DEGREE

Master of Science

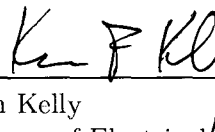
APPROVED, THESIS COMMITTEE:



Tomasz S. Tkaczyk, Chair
Assistant Professor of Bioengineering



Rebecca R. Richards-Kortum
Professor of Bioengineering



Kevin Kelly
Professor of Electrical and Computer
Engineering

Houston, Texas

May, 2010

UMI Number: 1486010

All rights reserved

INFORMATION TO ALL USERS

The quality of this reproduction is dependent upon the quality of the copy submitted.

In the unlikely event that the author did not send a complete manuscript and there are missing pages, these will be noted. Also, if material had to be removed, a note will indicate the deletion.



UMI 1486010

Copyright 2010 by ProQuest LLC.

All rights reserved. This edition of the work is protected against unauthorized copying under Title 17, United States Code.



ProQuest LLC
789 East Eisenhower Parkway
P.O. Box 1346
Ann Arbor, MI 48106-1346

ABSTRACT

Development of Image Mapping Spectrometer (IMS) for hyperspectral fluorescence
microscopy

by

Liang Gao

An image mapping spectrometer (IMS) for microscopy applications is presented. Its principle is based on the redirecting of image zones by specially organized thin mirrors within a custom fabricated component termed an image mapper. The demonstrated prototype can simultaneously acquire a 140nm spectral range within its 2D field of view from a single image. The spectral resolution of the system is 5.6nm. The FOV and spatial resolution of the IMS depend on the selected microscope objective and for the results presented is $45 \times 45 \mu^2$ and $0.45 \mu\text{m}$ respectively. The system requires no scanning and minimal post data processing. In addition, the reflective nature of the image mapper and use of prisms for spectral dispersion make the system light efficient. Both of the above features are highly valuable for real time fluorescent-spectral imaging in biological and diagnostic applications.

Content

Abstract	ii
1 Introduction	1
2 Operating principles of IMS system	6
3 Experimental demonstration of IMS operating principle by 1×5 Image mapper	8
3.1 Fabrication of first generation 1×5 image mapper	8
3.2 Experimental demonstration of operating principle of IMS	10
3.3 Preliminary imaging test results	11
4 Fabrication and characterization of 5×5 image mapper	12
4.1 Grouped 2D remapping design	12
4.2 Fabrication of 2D image mapper by raster fly-cutting method	14
4.3 Characterization of 2D image mapper	16
5 Optics design of reimaging lenses	19
6 IMS spectral imaging results	22
6.1 Image quality and PSF measurement of undispersed remapped resolution target	22
6.2 Fluorescent beads imaging experiment	24
7 Conclusions and future work	29

Chapter 1

Introduction

Fluorescence imaging is an indispensable tool for biological studies, especially in cellular research. Through the staining of cells with various fluorophores and imaging under a microscope, a large volume of color-coded processes can be quantitatively characterized, from chromosome dynamics [1] to gene expression [2]. The development of fluorescent probes has greatly improved cellular research by bringing high quantum yield fluorescent dyes and multiplexed staining methods into the field [3]. This has enabled researchers to investigate several organelles and their interactions in the same field of view (FOV) and at the same time with high contrast. As more and more fluorophores are developed in the visible light band, a central problem for multi-staining methods to solve is how to discriminate fluorescent probes with spectral peaks very close to each other. So in addition to the traditional requirements on spatial resolution, high spectral resolution is also necessary for imaging devices which target fluorescent imaging applications.

Hyperspectral fluorescence microscopy (HFM) is an emerging field based on hyperspectral or multispectral imaging concepts, which often borrow from remote sensing techniques [4, 5]. Because of its high spectral resolution (less than 10nm), HFM has found many applications in spectral imaging of living cells [6-9]. HFM has also been used to discriminate the contributions of autofluorescence from exogenous fluorescent signals present in the sample [10]. Compared to only 3 spectral bands that can be obtained by the traditional RGB color cameras or multi-filter imaging, HFM has the

capability to capture the whole fluorescent spectrum within its 2D FOV, and build a 3D datacube (x, y, λ) for multivariate data analysis. Such data can provide accurate information about fluorescent probe distributions and their relative concentration over the whole specimen.

On the other hand, HFM with high temporal resolution is gaining more importance in biological microscopy. This is because it can be used to capture transient scenes, which is often a critical requirement in cellular dynamics research. Unfortunately, most currently available HFMs need scanning which limits their temporal resolution. For example, hyperspectral confocal microscopy is a spatial scanning technique which can implement three-dimensional sectioning while providing spectral information. However, even state-of-art HFM/confocal systems can only acquire data at a rate up to 5 frames/s with 512×512 pixels [11]. HFM with an acousto-optic tunable filter (AOTF) or liquid crystal tunable filter (LCTF) is another technique based on spectral scanning [12, 13], which can switch wavelengths very fast. For HFM with AOTF, switching times are typically less than 100 microseconds [14]; for HFM with LCTF, around 50ms in the visible light band, and ~ 150 ms in NIR band [15]. However, there is a trade-off between the quantity of spectral bands captured and the total acquisition time. Plus, due to fairly poor throughput (the AOTF has transmission of $\sim 30\%$ in the visible light range [14]; LCTF can exhibit over 50% peak transmission for red and NIR light, but this number reduces to $\sim 15\%$ in the blue region [15]), these systems are not ideal candidates for fluorescent real-time imaging. In addition to the above HFM approaches, other scanning techniques include Fourier-transform imaging spectrometers [16] (scanning in phase space) and fiber Fabry-Perot arrays [17] (scanning in frequency). The scanning

mechanism of these HFMs still decreases their temporal resolution and limits their potential use in real-time imaging. To fully utilize the potential information yielded by fluorescent probes in HFM, snapshot techniques are needed.

Currently, many snapshot techniques have been developed for hyperspectral imaging, such as aperture splitting [18], field splitting (by fibers [19] or lenslet arrays [20]), Computed Tomography Imaging Spectrometry (CTIS) [21], and Coded Aperture Snapshot Spectral Imaging (CASSI) [22-23]. Among these, CTIS and CASSI are particularly interesting due to their higher throughput and compact size which are both critical features for fluorescence microscopy. CTIS has already been demonstrated in fluorescence microscopy [24] and CASSI has just recently been used in real-time spectral imaging for remote sensing applications [25] but has yet to be tested in microscopy. CTIS utilizes a computer-generated-hologram (CGH) to map multiple projections of the 3D data tube (x, y, λ) onto a 2D detector array. After being processed by linear algebra reconstruction methods, spectra from every spatial position within the CGH's two-dimensional FOV is collected. Although CTIS can provide spectral imaging of fast moving and/or low-light objects it suffers from many problems, including massive computational requirements and the missing cone effect. CASSI draws on the ideas of compressed sensing. The spatial modulation is brought in by a coded aperture, and is later transformed to spatial and spectral modulation in the undoing process. Then a multiscale reconstruction algorithm is employed to extract the spatial and spectral information from the mask-modulated intensity graph. However, this technique has limitations on spectrally resolving point sources. Beside these two, current aperture splitting and field splitting techniques also have defects. Aperture splitting is not light

efficient, while field splitting by fibers or lenslet arrays is limited by size of their spatial sampling components.

In this thesis, a novel snapshot HFM device is presented – the Image Mapping Spectrometer (IMS). It can acquire the whole spectral information within its FOV via a single integration of an array detector. By directly imaging the remapped and dispersed image zones onto a CCD detector, the IMS system overcomes the CTIS and CASSI's problems of computational reconstruction and resolution loss. The IMS acquires data directly with minimal post processing to build a 3D datacube.

Although the IMS concept has already been established in astronomical optics for over a decade [26-29], because of the characteristics of imaging objects (galaxies, stars, etc.), astronomical IMS systems have relatively low spatial sampling (typically less than 60 mirror facets) [30]. No current astronomical IMS system can be simply modified and adapted for the demanding requirements of biological fluorescence microscopy. To the best of our knowledge, this is the first time that the image mapping concept has been implemented for high-resolution microscopy.

Up to now, we have fabricated two generations of image mappers and built the corresponding optical systems. The first generation is 1×5 (tilts in x axis \times tilts in y axis) image mapper which only has 5 one dimensional tilts. We use this image mapper to experimentally demonstrate the operating principle of IMS; the second generation is 5×5 image mapper which has 25 two dimensional tilts. We implement this mapper into the optics and realize sampling the datacube at $100 \times 100 \times 25$ (x, y, λ). When coupling to a microscope which uses $40\times$ objective (N.A.=0.75) to image the sample, the new IMS

prototype realizes 0.45 microns and 5.6 nm resolution in spatial and spectral domains respectively. While the system presented here is a proof-of-concept device, if required, the instrument could be redesigned and built to a different specification to improve spatial and spectral resolution. The imaging results presented in chapter 6 demonstrate the promising potential of the IMS system in HFM research.

Chapter 2

Operating principles of IMS

The operating principle of the IMS system is shown in Fig. 2.1. An acinus cell image [31] formed at the side port of a microscope is first reimaged onto the image mapper – a custom made redirecting mirror. The image mapper is composed of many long strip mirror facets which reorganize the image to provide optically void regions on a large format CCD image sensor. The mirror facets of the image mapper have tilt angles that reflect the remapped image zones into different directions. In Fig. 2.1 the image mapper is shown as a simplified 3D model which has only 8 mirror facets, tilted in the two-dimensional direction (α_i, β_j) ($i, j=1, 2$). However, the real image mapper used in the system has much more mirror facets and tilt angles. Subsequently, a prism disperses the remapped image zones into their neighboring void regions. The remapped and dispersed image can be acquired in a single integration event on the CCD camera. This mapping method establishes a one-to-one correspondence between each voxel in the datacube (x, y, λ) and pixel on the CCD camera. Therefore it is possible to directly measure the distribution of light intensities in the object. The position-encoded pattern on the CCD camera contains the spatial and spectral information within the microscopic image, both of which can thus be obtained simultaneously. No reconstruction algorithm is required since the image data contains direct irradiance from the object. Simple image remapping is sufficient for image and data display.

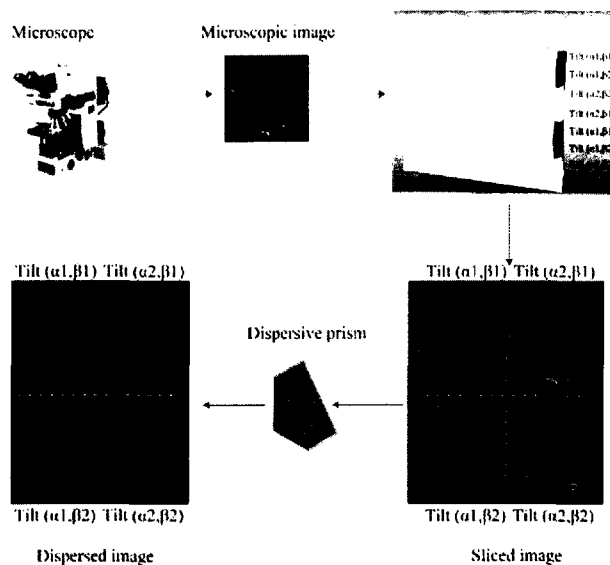


Fig. 2.1 The operating principle of the IMS system

The dimensions of the data cube obtained in the IMS depend on the size of the CCD image sensor. This means that the total number of voxels cannot exceed the total number of pixels on the CCD camera. Therefore for a given camera, one can always increase the spatial sampling at the expense of spectral sampling, and vice-versa. For example, by using a 1024×1024 pixel camera, a datacube (x, y, λ) can be built either in the $256 \times 256 \times 16$ format, or $512 \times 512 \times 4$ (the first two numbers describe spatial sampling, and the third one is the spectral sampling). To realize higher spatial and spectral sampling simultaneously, a large format CCD camera should be selected. The largest scientific grade CCD camera currently available is 16 Megapixels which limits the IMS to a datacube maximum of $500 \times 500 \times 60$. Consumer grade cameras have recently reached 25 megapixel resolutions which further extend the possible resolution of the IMS in the future.

Chapter 3

Experimental demonstration of IMS operating principle by 1×5 image mapper

The operating principle of IMS is conceptually illustrated in the Chapter 2. In this chapter, a 1×5 image mapper is fabricated and incorporated into the test setup. The field remapping principle is experimentally demonstrated by the preliminary bright-field imaging results.

3.1 Fabrication of first generation 1×5 image mapper

To demonstrate the feasibility of fabricating micro-scale mirror facets and concept of image remapping principle, the first generation image mapper was fabricated by raster fly-cutting on a Nanotech U250 Ultra-Precision Lathe (UPL). The first generation image mapper is designed to have only 5 one-dimensional tilts in order to simplify the fabrication process. The substrate was mounted on the base of Y axis of the UPL (See Fig. 3.1). A custom diamond flycutting tool made by Chardon Inc., (160 μ m tip width, 20.03° included angle) was mounted to the spindle of the lathe and rotates at a rate of 2800 rpm during the cutting process. When cutting process begins, the fly-cutting tool smoothly slides over the surface along X axis, removing materials along its path. The tilt angle of the mirror facet is determined by the depth of cut in Y axis. After completing a single mirror facet, the flycutting tool returns back and shifts a mirror facet width unit (160 microns) in Z axis and starts another pass until all the mirror facets are fabricated. The

fabricated parameters are shown in Table 3. 1. The finished image mapper is shown in Fig. 3.2.

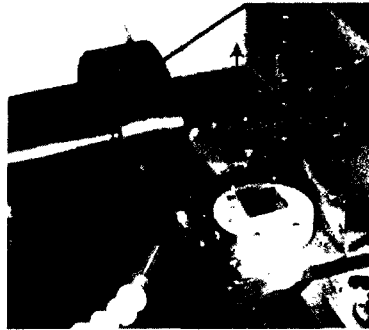


Fig.3.1 Fabrication of 1x5 image mapper

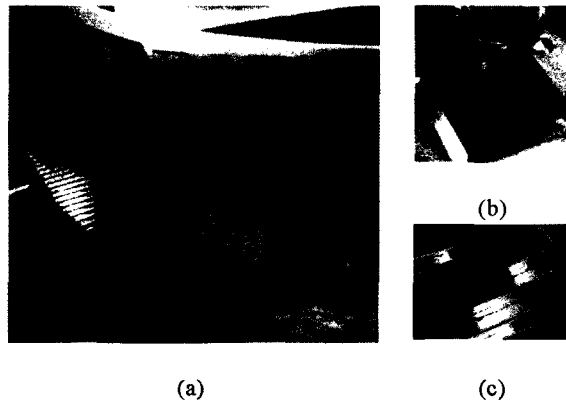


Fig. 3.2 (a) Picture of the first image mapper. (b) Image mapper with US Nickel for size reference. (c) Zygo NewView 5000 3D image of the center region of mirror facets 1-5, the false color shows depth information.

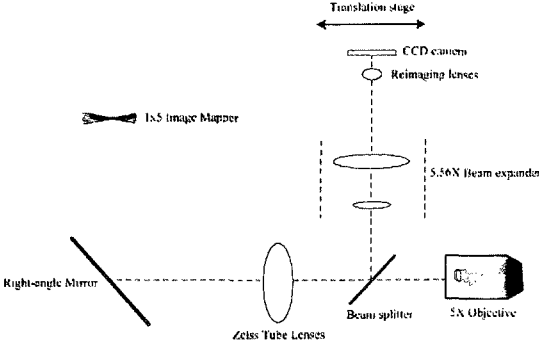
Table 3.1. Fabrication parameters for 1x5 image mapper

Tilt angles along Z axis	0, ± 0.05 radians, ± 0.01 radians
--------------------------	-------------------------------------------

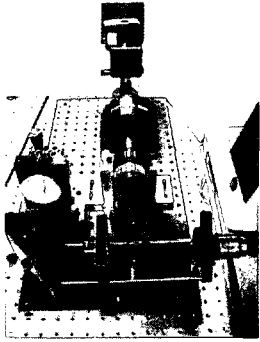
Effective substrate size	16mm×16mm
Mirror facet width	160 microns
Number of mirror facets	100

3.2 Experimental demonstration of operating principle of IMS

The schematic and system setup to implement 1×5 image mapper into the optics is shown in Fig. 3.3. The intermediate image which is formed at the microscope side port is first relayed onto the image mapper by a combination of 5x microscope objective & 130mm Zeiss Tube lenses. The image mapper takes the linear mapping of the field and reflects them back into 5 different directions. The reflected light is collected by the same Zeiss Tube lenses and form five pupils at its back pupil plane. A 5.56x beam expander is used to match the size of pupil with reimaging optics. Since this setup is mainly for demonstration of the field remapping principle, the parallel reimaging of all five pupils is replaced with sequential imaging with a single reimaging objective, and the dispersive element is not used to simplify the image reconstruction process.



(a) Schematics



(b) System setup

Fig. 3.3 Implementation of 1x5 image mapper into the optics

3.3 Preliminary imaging test results

Fig. 3.4 shows the pupil image and initial imaging experiments performed with the system prototype (Note that each separate pupil has two side lobes in the vertical direction due to the diffraction effect). A reimaging objective with focal length 160mm is mounted on a translation stage and moved manually to each separate pupil position, the corresponding separate image is captured by a CCD camera and shown in the arrow pointed position in Fig. 3.4. The void region between the image lines is created as expected. Because no dispersive element is used, the field can be regarded as monochromatic at final image plane. Thus, the image reconstruction process can be simply implemented by adding all five separate images together and forming an intensity combined image in Fig. 3.4 (f). The completeness and uniformity of the combined image over the whole FOV demonstrates the feasibility of the operating principle of IMS.

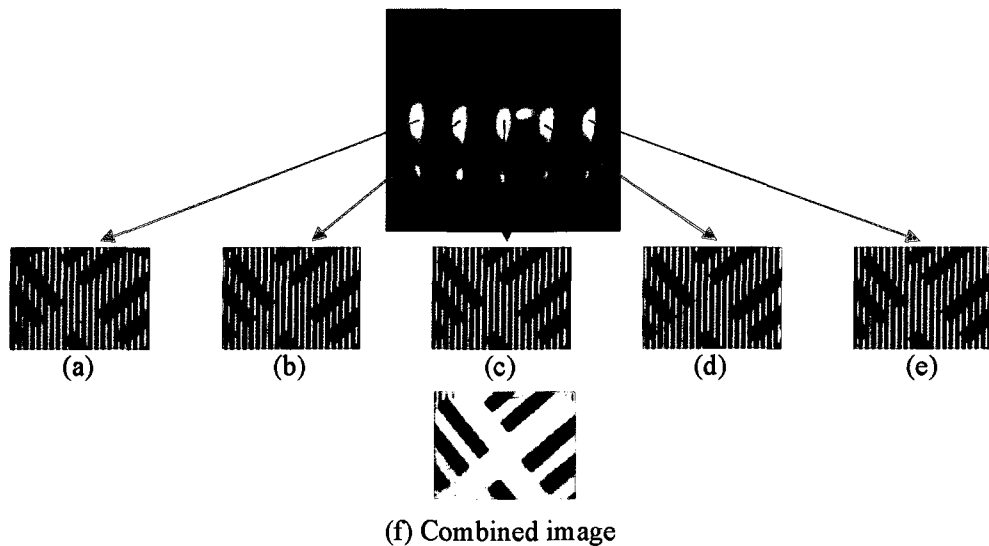


Fig. 3.4. Reimaging of 5 separate pupils and image reconstruction

Chapter 4

Fabrication and characterization of 5×5 image mapper

We have demonstrated the operating principle of IMS by 1×5 image mapper in chapter 3. However, the system can only realize 5 spectral sampling in the datacube. To build a system which has potential applications in HFM, we cut a 5×5 image mapper with two dimensional tilt angles. The 5×5 image mapper can sample the datacube at $100 \times 100 \times 25$ (x, y, λ). The fabrication of mirror facets follows the grouped 2D remapping design, which greatly simplifies the reimaging process. The grouped 2D remapping design and the fabrication & characterization of 5×5 image mapper will be presented in this chapter.

4.1 Grouped 2D remapping design

The image mapper is the most critical component in the IMS system. It plays the role of *remapping the field and redirecting the image zones into different pupils*. The image mapper is comprised of multiple mirror facets. The number of mirror facets (M), the length of the mirror facets in relation to the image PSF (N) (Note: The prototype is optics limited for the spatial resolution in this direction), and the number of tilt angles (L), determine the size $N \times M \times L$ of the 3D (x, y, λ) datacube. Note that N is the total number of spatial data points in the x -dimension, M is the total number of spatial data points in the y -dimension, and L is the total number of spectral data points (λ). In order to obtain the required void regions in the undispersed image, the mapper is composed of repeating blocks of mirror facets with L tilt angles as shown in Fig. 4.1 (a). For our prototype system, there are 25 total tilt angles (i.e. 25 spectral bands) labeled in red with an

accompanying arrow to indicate the direction of tilt. Each mirror facet within the block re-directs a part of the image within that block to a unique location in the pupil (Fig. 4.1 (b)) also labeled with the same red number as its corresponding tilt angle. The block is then repeated down the length of the mapper until all N mirror facets in the x direction have been obtained. In this manner, each pupil only sees every L_{th} line of the image corresponding to the same tilt angle (in both x and y directions). For our prototype system of $100 \times 100 \times 25$, each lens in the re-imaging array only sees a total of 4 image lines from the original image.

As the system is telecentric at the mapper's image side, the chief rays reflected by a specific mirror facet in each block have the same reflection angle. After passing the collecting lens, the light associated with these chief rays will enter the same pupil corresponding to a specific block. In this way, the reflected light from an entire mapper block gets separated into different pupils. Each reimaging lens is then dedicated to only one tilt direction and reimages all associated image lines. The image is thus efficiently re-distributed for spectral separation without losing any light. Note that this is an important improvement over previous astronomical image mappers which reimaged every image line separately, instead of in a common pupil location which simplifies the design and makes it more compact for high resolution microscopy applications. Using this approach the spatial and spectral resolution must be balanced for both the N.A. and FOV of the collecting lens (i.e. etendue). For the square pupil configuration, $(L/2)^{1/2} NA_{mapper} \leq NA_{collect}$ where $NA_{collect}$ is the N.A. of the collecting lens and NA_{mapper} is the N.A. exiting the image mapper. The $NA_{collect}$ limits the spectral resolution of the system

while the FOV determines the spatial resolution of the system (i.e. # of mirror facets in the FOV).

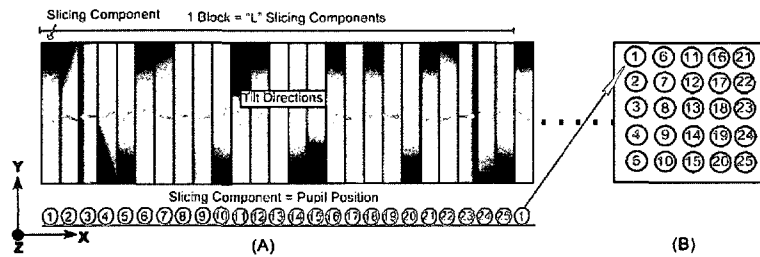


Fig. 4.1. Pupil selection principle. Fig. (a) shows one of the image mapper's repeating blocks, and Fig. (b) shows the corresponding pupil plane. In (a) the arrow in each mirror facet represents the tilt direction (there is no arrow on mirror facet 13 because it has no tilt) and the sequential number represents the mirror facet index. Light reflected from each mirror facet in this block will enter the corresponding pupil in (b). The dimensions of mirror facets in the Fig. are scaled to show their features. In the prototype, the mirror facet is 16mm in length (Y direction), and 160 μ m in width (X direction).

4.2 Fabrication of 2D image mapper by raster fly-cutting method

The image mapper can be fabricated with several technologies, such as raster flycutting, micro-milling, or lithography [32, 33]. For this prototype, the image mapper was made by raster flycutting on a Nanotech U250 Ultra-Precision Lathe (UPL), which can be later reproduced with molding for mass production. The Nanotech U250 UPL is a 4 axes (X, Y, Z and C) lathe which allows diamond turning, micro-milling and raster flycutting at high sub-micron precision and 1-10 nanometer scale roughness. The image mapper substrate used for the IMS prototype is made of high purity aluminum. The substrate was placed on a manual goniometer (Newport GON40-U, 0.0022° sensitivity) which was fixed to the base of Y axis of the UPL. A custom diamond flycutting tool made by Chardon Inc., (160 μ m tip width, 20.03° included angle) was mounted to the spindle of the lathe and rotates at a rate of 2800 rpm during the cutting process. The mirror facets

are designed to have tilts around the Z axis and the X axis in the machine coordinates (See Fig. 4.2). The tilt angles of the mirror facets can be described by two parameters: The first one is the tilt angle α around the Z axis which is controlled by the depth of cut of the flycutting tool. And the second one is the tilt angle β around X axis which is controlled by the rotation angle of the goniometer.

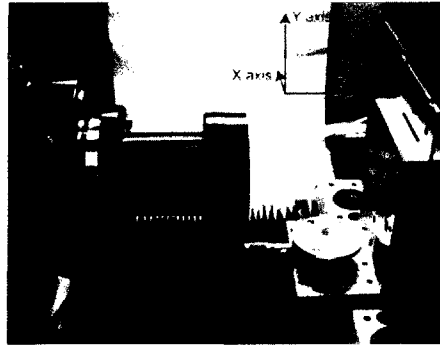


Fig. 4.2. Raster flycutting on Nanotech 250UPL. Red coordinate arrows indicate the X, Y, and Z axes of the machine. C axis is not used in raster flycutting mode.

When cutting process begins, the rotation angle of goniometer is first set to 0.46° with respect to the horizontal plane. Then the flycutting tool smoothly slides over the surface along the X axis, removing materials along its path. After completing a single mirror facet, the flycutting tool returns back and shifts a mirror facet width unit (160 microns) in Z axis and starts another pass until all the mirror facets in a block with tilt angle $\beta=0.46^\circ$ (called a mapper section) are fabricated. Then the flycutting tool shifts a block width unit (4mm) in Z axis to cut the next block. By just shifting the origin's Z coordinate the distance of a mapper section width (0.8mm) after each change of goniometer angle, the whole process is repeated for $\beta=0.46^\circ, 0.23^\circ, 0^\circ, -0.23^\circ, -0.46^\circ$ sequentially. The preset parameters for the finished image mapper are shown in Table 4. 1.

Table 4.1. Fabrication parameters for image mapper

Tilt angle α along Z axis	$0, \pm 0.23^\circ, \pm 0.46^\circ$
Tilt angle β along X axis	$0, \pm 0.23^\circ, \pm 0.46^\circ$
Mirror facet width	160 microns
Mirror facet length	16mm
Mirror facet number	100

4.3 Characterization of 2D image mapper

A photographic picture of the fabricated image mapper prototype is shown in Fig. 4.3(a) and Fig. 4.3(b), and a three dimensional profile of a portion of the image mapper acquired with a white light interferometer is shown in Fig. 4.3(c).

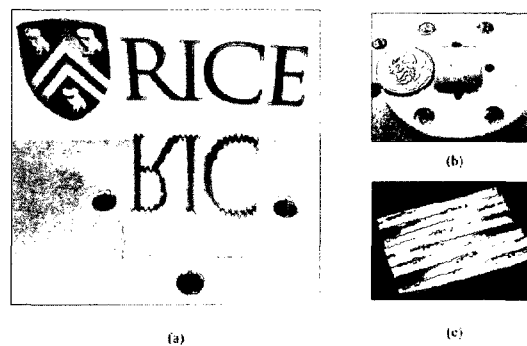


Fig. 4.3. The profile of image mapper. Fig. (a) and (b) are photographic pictures. In (a), the remapped Rice logo letters can be directly seen in the reflection direction. In (b), a quarter is placed as the reference to show the size of the image mapper ($16\text{mm} \times 16\text{mm}$). Fig. (c) is a three dimensional picture of a portion of the image mapper obtained by Zygo white light interferometer.

The tilt angle and surface roughness of each mirror facet was measured using the Zygo NewView 5032 (Fig. 4.3(c)) white light interferometer. The accuracy of the tilt angle measurement of the interferometer is 0.01° . The tilt angles of 25 mirror facets in a block

were also measured. The measured value presented in Table 4.2 was obtained by averaging the five mirror facets in a block with the same α or β expected value. Generally speaking, α is closer to the expected value than β . This is because β is controlled by the manual goniometer. For the current low sampling IMS prototype, the reimaging optics can be designed to accommodate these tolerances. But for a future high resolution IMS system stricter angle tolerances will be required and the manual goniometer may not be suitable anymore and should be replaced by a more precise motorized one.

Table 4.2. Mirror facet tilt angle measurement

Expected Value	Measured α	Measured β
-0.46°	$-0.456^\circ \pm 0.0055^\circ$	$-0.44^\circ \pm 0.0255^\circ$
-0.23°	$-0.224^\circ \pm 0.0114^\circ$	$-0.226^\circ \pm 0.0114^\circ$
0°	$0.008 \pm 0.0084^\circ$	$0.024^\circ \pm 0.0167^\circ$
0.23°	$0.242^\circ \pm 0.0084^\circ$	$0.27^\circ \pm 0.02^\circ$
0.46°	$0.472^\circ \pm 0.0084^\circ$	$0.526^\circ \pm 0.0055^\circ$

To obtain the surface roughness data, a virtual mask is applied to make only one mirror facet visible in the FOV ($0.14\text{mm} \times 0.11\text{mm}$). Roughness is measured at three randomly picked up mirror facets. An average of 6nm RMS value indicates their good surface quality. In Fig. 4.4, a 3D height profile of a mirror facet is shown. Based on the high purity nature and surface smoothness, for example, the percent decrease in specular reflectance due to the surface roughness is only $\sim 2\%$ [34], the reflectivity of the mirror facet is expected to be comparable to that of evaporated aluminum film, which is above 90% in the visible light range [34].



Fig. 4.4. Mirror facet surface height profile. The roughness data is obtained by the removal tilt. Surface roughness RMS value = 6 nm.

Chapter 5

Optics design of reimaging lenses

In this $100 \times 100 \times 25$ (x, y, λ) IMS prototype, the reimaging lens sets are assembled using off-the-shelf achromatic doublets (60mm F.L. doublets and -12.5 F.L. doublets). They are arranged as 5×5 array pattern. Custom opto-mechanics were designed and fabricated to support these lenses (See Fig. 5.1). The opto-mechanics were black anodized to reduce any stray light effects in the system. The optical design for each reimaging lens set in the array was modeled using ZEMAX to verify diffraction limited performance over the full field of view (FOV) and spectral range (See Fig. 5.2).

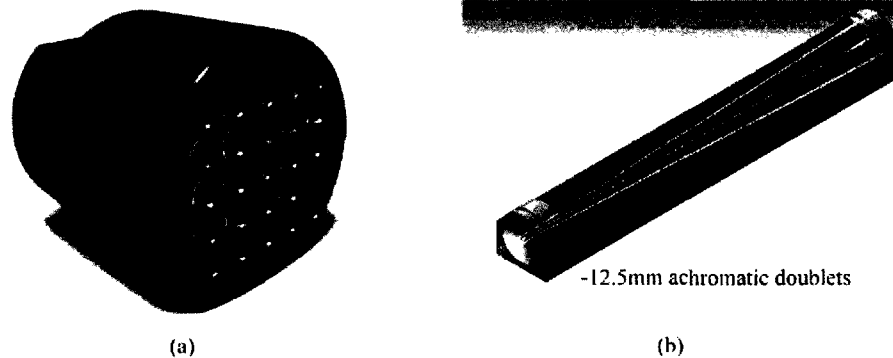


Fig. 5.1. Reimaging lenses and mount. Fig. (a) shows the photographic picture of the whole piece. There are 25 tubes inside this mount. Each tube holds a reimaging lens set. Fig. (b) gives the cross section view of a single tube. 60mm F.L. achromatic doublets are mounted at the back of the tube (facing the pupil), while -12.5mm F.L. achromatic doublets are mounted at the front of tube (facing the image plane). The F.L. of this reimaging lens set is 350mm.

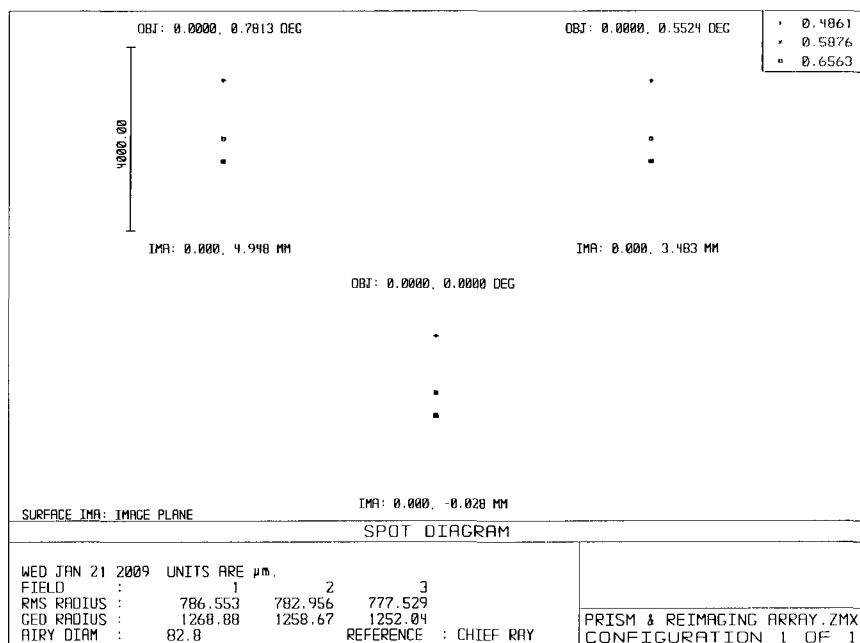


Fig. 5.2. Zemax simulation of optical performance of reimaging lenses. The black circle represents the airy disk for reference.

The FOV of a reimaging lens set is designed to be overlapped with adjacent lens sets to maximize the usable area of the CCD camera. As the whole mapper plate's image has a square shape, while the FOV of the reimaging lens set is circular, there exist four void regions outside the mapper plate's image but inside the FOV (See Fig. 5.3). Because of these void regions, the FOV of neighboring reimaging lens sets are allowed to overlap. This allows a fully utilized imaging area on the CCD camera.

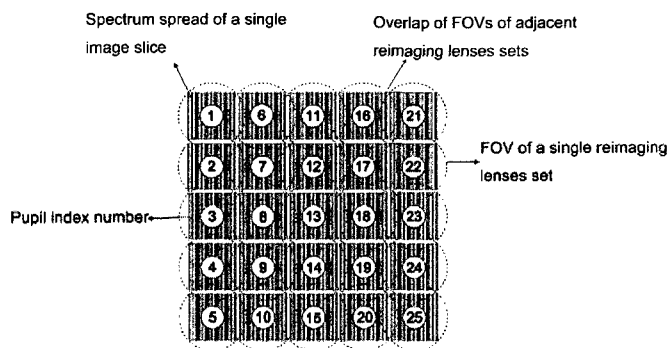


Fig. 5.3. Overlap of the FOVs on the CCD camera. Each reimaging lens set images the corresponding pupil in the pupil plane. The FOVs of adjacent reimaging lens are overlapping to fully utilize the CCD area. The image mapper itself creates a field stop allowing the overlap.

Chapter 6

IMS spectral imaging results

In order to verify the image performance and test the spatial and spectral resolution of the IMS prototype, imaging experiments were performed in the following sequence: (1) the undispersed 1951 USAF resolution target was imaged and the PSF (point spread function) of a single image line was measured; (2) spectra images of test samples made with fluorescent beads were obtained.

6.1 Image quality and PSF measurement of undispersed remapped resolution target

An image of an undispersed 1951 USAF resolution target was obtained by removing the prism from the instrument. The target is placed on the microscopic stage. The raw image was captured with a 16-bit CCD camera without binning (pixel size equal to $9\mu\text{m}$). To calibrate the spatial features in the image, first a black bar across the whole FOV is chosen for imaging. Then, the image lines are aligned with each other manually to restore the straight bar feature. At the same time, the starting coordinates of each image line on the camera are recorded. A “jigsaw puzzle” algorithm was developed to build the system realignment matrix. By imposing this matrix on the target raw data, the image can be reconstructed automatically. Note that image registration and distortion are allowed in the raw image because they will be calibrated out of the system during this process. To calibrate the image intensity, another reference blank image was obtained under uniform illumination and with no object on the microscope stage. After dividing the intensity data

at each target image line by the corresponding value at the reference image line, the target image intensity is corrected.

The smallest feature of USAF target was moved to the center of FOV to test the image quality of the reconstructed image. The reconstructed result from the raw data (See Fig. 6.1 (a)) is shown in Fig. 6.1(b). The width of the top black bars presented in the Fig. is 2.19 μm . Fig. 6.1(c) shows the direct image of the same bars at the microscope side port for comparison (captured by Lumenera Infinity1-1 monochromatic camera). The imaging results demonstrate that the prototype can image microscopic samples with contrast $(I_{\text{max}}-I_{\text{min}})/(I_{\text{max}}+I_{\text{min}})\approx 0.5$ for the 2.19 μm bars in Fig. 6.1(b), which corresponds closely to the direct imaging result. The PSF of the IMS was measured by analyzing the intensity distribution of a line that is across a single image line (See Fig. 6.2). The FWHM is about 7 pixels, which is 63 μm . The theoretical N.A. at the camera's side is 0.005, corresponding to a diffraction spot size of 122 μm (FWHM of diffraction limit is 61 microns). This suggests that the IMS system approaches the diffraction limit. The distance between the peaks of two adjacent undispersed image lines is also measured to be around 170 pixels. It indicates that about 24.3 spectral bands can be resolved within the void regions and is very close to the 25 spectral bands designed for.

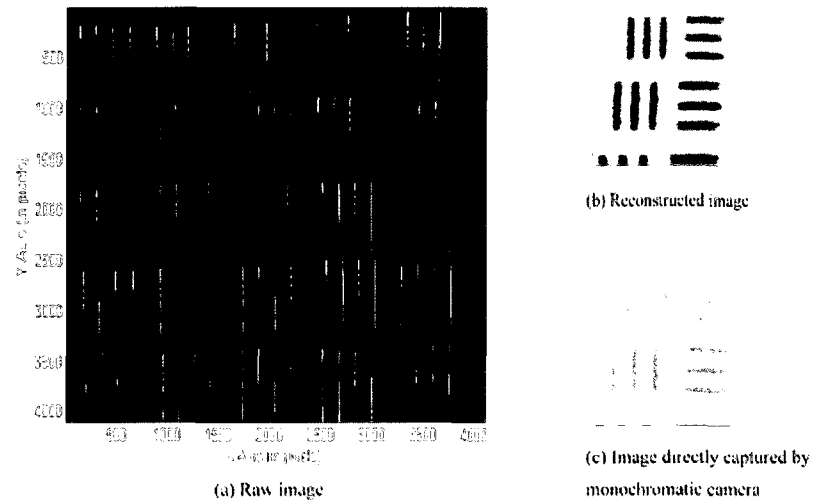


Fig. 6.1. A 1951 USAF target undispersed image. The raw image (a) is obtained using a 16-bit camera without binning (pixel size = $9\mu\text{m}$). Fig. (b) is the reconstructed image. For comparison purposes, an image of the same bars is captured at the microscope side port directly using a monochromatic camera. The imaging result is shown in Fig. (c). The top bars in the FOV belong to Group 7, Element 6 (bar width = $2.19\mu\text{m}$).

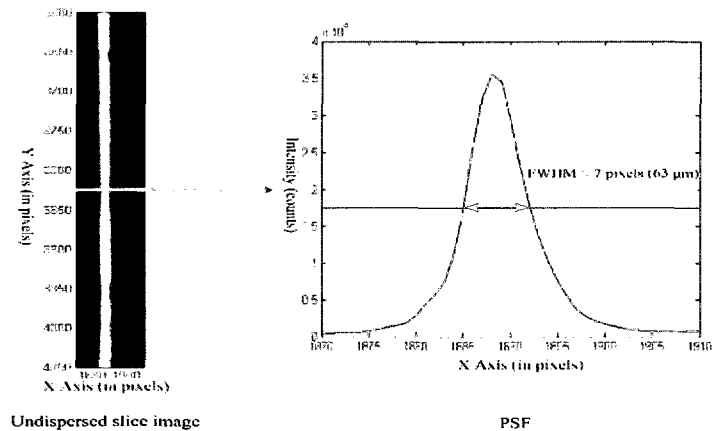


Fig. 6.2. The PSF of a single image line from an undispersed image. The camera pixel size equals $9\mu\text{m}$. The x and y positions indicate the location of this image line in the CCD camera's global coordinates.

6.2 Fluorescent Beads imaging experiment

6.2.1 Sample preparation

Before imaging, the fluorescent beads were uniformly suspended by vortex mixing and sonicating the suspension. One drop of suspension was added to 1ml buffered saline solution to be diluted. Then the diluted suspension was deposited onto a microscope slide and sealed by a coverslip. Two samples were prepared for the IMS imaging test. One contains only the green beads, while the other is a mix of yellow and red ones.

6.2.2 Imaging results

Images of the fluorescent beads are shown in Fig. 6.3 and Fig. 6.4. Chroma filter sets (61001 and 31002) were used to select the excitation wavelength and separate the fluorescent signal from the excitation light. Filter set 61001 (DAPI/FITC/PI) was used for fluorescent imaging of the green beads; Filter set 31002 (TRITC/DiI/Cy3) was used for fluorescent imaging of the red & yellow mixed beads). The diameter of these fluorescent beads is around $2.5\mu\text{m}$. The raw image was captured with the 16-bits camera under 4×4 binning working mode (binned pixel size equal to $36\mu\text{m}$). Note that the magnification of the prototype is not optimized for the pixel size and therefore requires longer integration times. In the future the same CCD will be used for larger format, optimized IMS and we predict integration times to be 16 to 64 times shorter. Currently, however to fully utilize the dynamic range of the camera, the integration time is set to be 2s to obtain the spectrum of yellow & red beads, and 6s to acquire the spectra of green beads. Full dynamic range is used here because high contrast imaging is preferable in this experiment. It can provide a high contrast fluorescent beads image with maximum spatial and spectral resolution. Users can increase the imaging speed based on their own contrast preferences. For example, if 8 bits dynamic range is used instead of 16 bits, the integration time for the green fluorescent beads are expected to be about 20ms. Users

can also use higher illumination level to increase the sample brightness to reduce the necessary integration time. The solid blue line in the spectrum diagram is obtained by the IMS prototype, while the red crosses dotted line is obtained by the Ocean Optic USB4000 spectrometer for comparison. Because this prototype is designed to demonstrate the principle, basic spectral calibration is carried out here. For initial spectral calibration, four wavelengths and their corresponding pixel locations were used. The first three wavelengths (500 nm, 550 nm, and 600 nm) come from narrow band filters (10nm bandwidth) placed in front of the microscope's broadband halogen lamp. The fourth wavelength comes from the fluorescent bead's peak spectrum as measured by the USB4000 spectrometer. Linear interpolation is used between these wavelength locations to estimate the other wavelength/pixel correspondences. The spectral shape of both measurements overlaps well and demonstrates the capability of the IMS prototype for performing fluorescent spectral imaging. Note that although the calibration is quite basic here, the spectral data obtained with IMS system matches very well with the reference spectrum. More precise and quantitative spectral data are expected to be obtained in future IMS systems when complete and thorough calibration procedures are adopted.

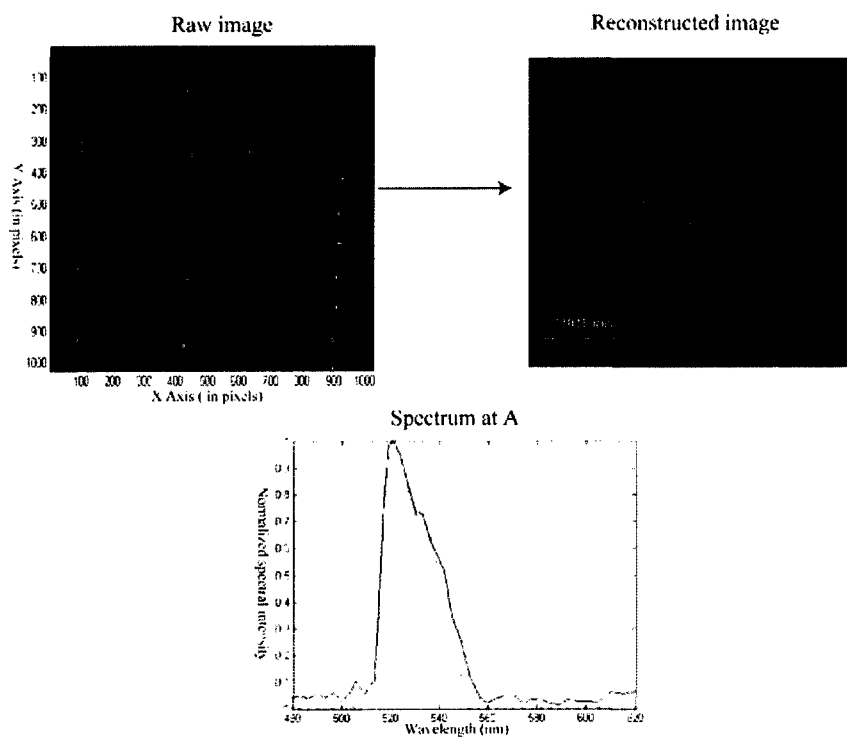


Fig. 6.3. IMS images of green fluorescent beads. The raw image is obtained using a 16-bit CCD camera with 6s integration time. The bead's spectrum is obtained from point A in the re-constructed image.

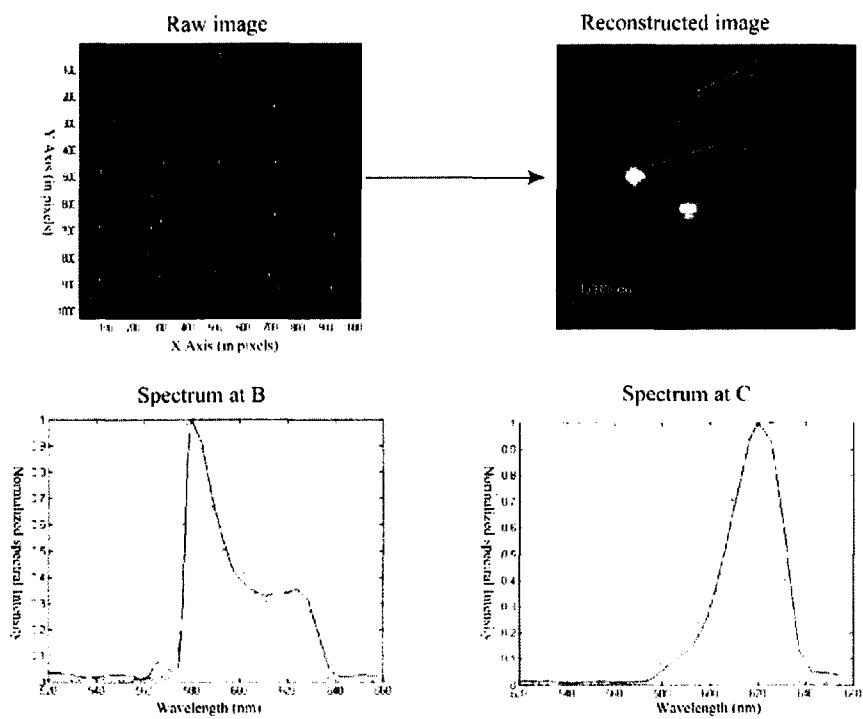


Fig. 6.4. IMS images of red and yellow fluorescent beads. The raw image is obtained using a 16-bit CCD camera with 2s integration time. The yellow bead's spectrum is from point B in the re-constructed image and the red bead's spectrum is from point C in the re-constructed image.

Chapter 7

Conclusions and future work

We have presented a proof-of-concept snapshot IMS for microscopic applications. The prototype is a compact and compatible instrument that can be coupled to many modalities, such as microscopes, endoscopes and other. It has realized $100 \times 100 \times 25$ sampling in the 3D datacube (x, y, λ) , corresponding to $0.45 \mu\text{m}$ spatial and 5.6nm spectral resolution respectively when a $40 \times / \text{N.A.} = 0.75$ objective is used on the microscope. The FOV, spectral range, spatial and spectral resolution can be easily tuned to cater to the specific needs of biological imaging. In this prototype, an off-the-shelf Zeiss tube lens is used as the collecting lens (25 mm FOV, 0.033 N.A.). Such optics set a spectral sampling limit at 25. To build higher spectral sampling IMS systems, custom made and assembled lenses may be needed to be used to effectively collect and reimaging light onto the CCD camera.

The design and fabrication of the image mapper used in this prototype is an important improvement, compared to previous astronomical mappers. First, the width of mirror facet used in this IMS system is only 160 microns which allows sampling at high density. Additionally the use of micro-facets shrinks the volume of the entire system to a compact table-top or potentially smaller dimensions needed for biological applications. For future higher spatial sampling IMS systems, smaller width cutting tools will be adopted to fabricate even thinner mirror facets. This will help the IMS to reach higher spatial resolution in a fixed FOV. Diffraction is an inevitable effect and should be seriously considered when small mirror facets are used. When mirror facets sample the diffraction

spot at the image side, some reflected rays will deviate from geometrical optical path and leak into adjacent pupils on the pupil plane, which can lead to crosstalk between neighboring array images. Crosstalk might become one of major background noises and affect the accuracy of spectral measurement, especially for those stained samples emitting strong and weak fluorescent signals simultaneously. While this is a concern it can be compensated with cutting larger tilt angle mirror facets and separating array components more. The theoretical and experimental analysis of crosstalk is currently being investigated in our group. A Fourier transform based diffraction analysis predicts the presented prototype experienced crosstalk of approximately 1.0% level. Experimental result shows this value is between 2% to 8%, which is obtained by measuring the ratio of the intensity of the ghost image to that of the primary image in the FOV of the same reimaging lenses set. Beside diffraction, other image artifacts include neighboring mirror facet's side walls shadowing other mirror facets and mirror facet edge eating effect, which are both coming from the depth of cut and the included angle of the cutting tool. These artifacts contribute little to the image quality in the current mapper configuration. For example, the edge eating percent is estimated to be under 7%; shadowing is negligible because the incident angles of light are less than the tilt angle of side walls. But they may become a serious problem when mapper with narrow width and bigger tilt angles are used for future higher resolution systems.

The building of the reimaging lens array to image separated pupils is another innovative point for this prototype. Grouping tilt angles allowed simplifying the reimaging optics and overall system layout. The overlapped FOVs design enables efficient usage of the CCD's imaging area. As mentioned before the final restriction for the

sampling density of the datacube comes from the total number of imaging pixels on the CCD image sensor. Therefore the FOVs of each reimaging lens set should be efficiently arranged to fully utilize the imaging capacity of the camera.

In summary, the IMS system is a snapshot technique that can directly capture the spatial and spectral information within its FOV simultaneously. Limited post processing – re-mapping is sufficient as light intensity in each pixel corresponds to position and wavelength in the object. IMS system has a promising perspective and has a great potential to become an important modality for biological fluorescent imaging which requires high spatial, spectral and temporal resolution at the same time.

Reference

1. A. S. Belmont, "Visualizing chromosome dynamics with GFP," *Trends Cell Biol.* 11(6), 250–257 (2001).
2. S. M. Janicki, T. Tsukamoto, S. E. Salghetti, W. P. Tansey, R. Sachidanandam, K. V. Prasanth, T. Ried, Y. Shav-Tal, E. Bertrand, R. H. Singer, and D. L. Spector, "From silencing to gene expression: real-time analysis in single cells," *Cell* 116(5), 683–698 (2004).
3. M. A. Rizzo, and D. W. Piston, "Fluorescent Protein Tracking and Detection in Live Cells," in *Live Cell Imaging: A Laboratory Manual*, D. Spector and R. Goldman, eds. (Cold Spring Harbor Lab Press, Cold Spring Harbor, NY, 2004).
4. F. A. Kruse, "Visible-Infrared Sensors and Case Studies," in *Remote Sensing for the Earth Science: Manual of Remote Sensing (3rd ed.)*, Renz and N. Andrew, eds. (John Wiley & Sons, NY, 1999).
5. D. Landgrebe, "Information Extraction Principles and Methods for Multispectral and Hyperspectral Image Data," in *Information Processing for Remote Sensing*, C. H. Chen, ed. (World Scientific Publishing Company, River Edge, NY, 1999).
6. T. Zimmermann, J. Rietdorf, and R. Pepperkok, "Spectral imaging and its applications in live cell microscopy," *FEBS Lett.* 546(1), 87–92 (2003).
7. Y. Hiraoka, T. Shimi, and T. Haraguchi, "Multispectral imaging fluorescence microscopy for living cells," *Cell Struct. Funct.* 27(5), 367–374 (2002).
8. V. L. Sutherland, J. A. Timlin, L. T. Nieman, J. F. Guzowski, M. K. Chawla, P. F. Worley, B. Roysam, B. L. McNaughton, M. B. Sinclair, and C. A. Barnes, "Advanced imaging of multiple mRNAs in brain tissue using a custom hyperspectral imager and multivariate curve resolution," *J. Neurosci. Methods* 160(1), 144–148 (2007).
9. W. F. J. Vermaas, J. A. Timlin, H. D. T. Jones, M. B. Sinclair, L. T. Nieman, S. W. Hamad, D. K. Melgaard, and D. M. Haaland, "In vivo hyperspectral confocal fluorescence imaging to determine pigment localization and distribution in cyanobacterial cells," *Proc. Natl. Acad. Sci. U.S.A.* 105(10), 4050–4055 (2008).
10. D. M. Haaland, J. A. Timlin, M. B. Sinclair, M. H. V. Benthem, M. J. Matinez, A. D. Aragon, and M. W. Washburne, "Multivariate curve resolution for hyperspectral image analysis: applications to microarray technology," in *Spectral Imaging: Instrumentation, Applications, and Analysis*, R. M. Levenson, G. H. Bearman, and A. Mahadevan-Jensen, eds., *Proc. SPIE* 2959, 55–66 (2003).
11. C. Zeiss, Germany, "LSM 510 META Product Brochure". <http://www.zeiss.com>.

12. V. Ntziachristos, J. Ripoll, L. V. Wang, and R. Weissleder, "Looking and listening to light: the evolution of whole-body photonic imaging," *Nat. Biotechnol.* 23(3), 313–320 (2005).
13. R. Lansford, G. Bearman and S. E. Fraser, "Resolution of multiple green fluorescent protein color variants and dyes using two-photon microscopy and imaging spectroscopy," *J. Biomed. Opt.* 6, 311-318 (2001).
14. ChromoDynamics, Inc., Orlando, FL, "HSi-300 Hyperspectral Imaging System Data Sheet". <http://www.chromodynamics.net/>.
15. Cambridge Research and Instrumentation, Inc., Cambridge, MA, "VARISPEC Liquid Crystal Tunable Filters Brochure". <http://www.cri-inc.com/>
16. Z. Malik, D. Cabib, R. A. Buckwald, A. Talmi, Y. Garini, S. G. Lipson, "Fourier transform multipixel spectroscopy for quantitative cytology," *J. Microsc.* 182, 133-140 (1996).
17. D. Y. Hsu, J. W. Lin and S. Y. Shaw, "Wide-range tunable Fabry-Perot array filter for wavelength-division multiplexing applications," *Appl. Opt.* 44, 1529-1532 (2005).
18. S. A. Mathews, "Design and fabrication of a low-cost, multispectral imaging system," *Appl. Opt.* 47, 71-76 (2008).
19. H. Matsuoka, Y. Kosai, M. Saito, N. Takeyama and H. Suto, "Single-cell viability assessment with a novel spectro-imaging system," *J. Biotechnol.* 94, 299-308 (2002).
20. A. Bodkin, A. I. Sheinis and A. Norton, "Hyperspectral imaging systems," U. S. Patent 20060072109A1 (2006).
21. B. K. Ford, C. E. Volin, S. M. Murphy, R. M. Lynch and M. R. Descour, "Computed Tomography-Based Spectral Imaging For Fluorescence Microscopy," *Biophys. J.* 80, 986-993 (2001).
22. M. E. Gehm, R. John, D. J. Brady, R. M. Willett, and T. J. Schulz, "Single-shot compressive spectral imaging with a dual-disperser architecture," *Opt. Express* 15 14013-14027 (2007).
23. A. Wagadarikar, R. John, R. Willett and D. J. Brady, "Single disperser design for coded aperture snapshot spectral imaging," *Appl. Opt.* 47, 44-51 (2008).
24. B. Ford, M. Descour and R. Lynch, "Large-image-format computed tomography imaging spectrometer for fluorescence microscopy," *Opt. Express* 9, 444-453 (2001).
25. A. A. Wagadarikar, N. P. Pitsianis, X. Sun and D. J. Brady, "Video rate spectral imaging using a coded aperture snapshot spectral imager," *Opt. Express* 17, 6368-6388 (2009).

26. L. Weitzel, A. Krabbe, H. Kroker, N. Thatte, L. E. Tacconi Garman, M. Cameron and R. Genzel, "3D: The next generation near-infrared imaging spectrometer," *Astron. Astrophys. Suppl. Ser.* 119, 531-546 (1996).
27. S. Vives and E. Prieto, "Original image slicer designed for integral field spectroscopy with the near-infrared spectrograph for the James Webb Space Telescope," *Opt. Eng.* 45, 093001 (2006).
28. F. Henault, R. Bacon, R. Content, B. Lantz, F. Laurent, J. Lemonnier and S. Morris, "Slicing the universe at affordable cost: the quest for the MUSE image slicer," *Proc. SPIE* 5249, 134-145 (2004).
29. J. A. Smith, "Basic principles of integral field spectroscopy," *New Astron. Rev.* 50, 244-251 (2006).
30. F. Laurent, F. Henault, E. Renault, R. Bacon and J. Dubois, "Design of an Integral Field Unit for MUSE, and Results from Prototyping," *Publ. Astron. Soc. Pac.* 118, 1564-1573 (2006).
31. "Mechanisms of 3D intercellular signaling in mammary epithelial cells in response to low dose, low-LET radiation: Implications for the radiation-induced bystander effect," *Biological Sciences Division Research Highlights, Pacific Northwest National Laboratory* (2004). <http://www.pnl.gov/>
32. W. Preuss, K. Rickens, "Precision machining of integral field units," *New Astron. Rev.* 50, 332-336 (2006).
33. C. M. Dubbeldam, D. J. Robertson, D. A. Ryder and R. M. Sharples, "Prototyping of Diamond Machined Optics for the KMOS and JWST NIRSpec Integral Field Units," in *Optomechanical Technologies for Astronomy*, E. Atad-Ettinger, J. Antebi, D. Lemke, eds., *Proc. SPIE* 6273, 62733F (2006).
34. H. E. Bennett, J. M. Bennett and E. J. Ashley, "Infrared Reflectance of Evaporated Aluminum Films," *J. Opt. Soc. Am.* 52, 1245-1250 (1962).